# Design and Optimization of a TEM Coaxial Horn for Wideband Operation in Millimeter Waves

Elígia Simionato, Rafael A. Penchel, Sandro R. Zang and Ivan Aldaya

***Abstract*— This work explores a framework of numerical techniques to design a wideband TEM coaxial horn for millimeter waves operation. Firstly, aperture dimensions and flare angle were determined to avoid nulls in vertical radiation pattern at $\theta_{\mathbf{F}} < \mathbf{55^o}$. Then, a transition to a 2.92mm connector and a dielectric support for the central conductor are proposed. To enhance electromagnetic performance, Genetic Algorithm (GA) was used to optimize the transition and support dimensions. To address the antenna performance, full-wave electromagnetic analysis based on Finite Element Method was employed. The designed model presented frequency bandwidth larger than 45% (25-40 GHz) with return loss greater than 20dB.**

***Keywords*— Millimeter Waves, Coaxial Horn, Wideband Antennas**

## I. Introduction

The new daring demands for the next generations of mobile communications (5G, 6G and beyond) were introduced as a path to support countless emerging use cases with a high variety of applications and variability of their performance, delivered across a fully heterogeneous environment and across a wide range of devices [1]. Properly sustaining the growth of connected devices expected for the upcoming technological innovations will require managing the frequency spectrum, once the frequencies below 30GHz are already crowded [2]. The 30 to 300GHz range, referred to as millimeter-wave (mm-Wave) band, is an interesting alternative to the development of technology reliant on higher data rates due to allowing for larger bandwidth allocations, furthermore, promising applications at mmWave include not only communications but also wireless cognition, sensing, imaging and positioning [3]. However, there are a few constraints to overcome to operate in mm-Wave, i. e. great sensitivity to blockage by obstacles due to weak diffraction ability, and higher free-space path loss compared with lower frequency communications systems [4], [5].

In order to provide omnidirectinal coverage at mm-Wave frequency, a large number of designed antennas have been proposed [6], [7], [8], [9]. An option able to provide high gain and wideband behavior are the omnidirectional dual-reflector antennas fed by a TEM (Transverse Electromagnetic) coaxial horn [10], [11], [12], [13]. For these antennas, the gain is strongly dependent on the aperture's electrical size while the wideband behavior is dictated by the feeder [14].

A complete model of a coaxial horn was presented in [11] with frequency bandwidth of 30%. The antenna features a transition between the cylindrical region and a N-type connector (with typical frequency range up to 11GHz) and a mechanical structure to support the inner conductor. However, the geometry of the inner conductor support - a dielectric ring - leads to a complex manufacturing process in which two parts need to be constructed separately and joined later after the dielectric is inserted [11]. A similar model for the coaxial horn for 26 to 40 GHz was explored in [13] not including a transition region and a support. Furthermore, the radiation pattern for the horn in [13] presented a first null at a $\theta = 50^\circ$ elevation angle, which leads to a insufficiently illuminated antenna reflector, degrading the antenna's performance.

In this work we present the complete design of a coaxial horn (see Fig. 1) optimized to work in the $K_a$ frequency band (26GHz – 40GHz). After re-designing the aperture dimensions and flare angle of the model presented in [13] to avoid nulls in vertical radiation pattern at $\theta < 55^o$, a novel transition region for a standardized feed access (2.92mm K connector) and a novel support geometry that offers minimal manufacturing obstacles and reflection coefficient below $-20$dB was proposed. The final designed model presents a frequency bandwidth larger than 45% (25-40 GHz) with return loss greater than approximately 22dB and stable radiation pattern that properly illuminates the sub-reflector of omnidirectional dual-reflector antennas.

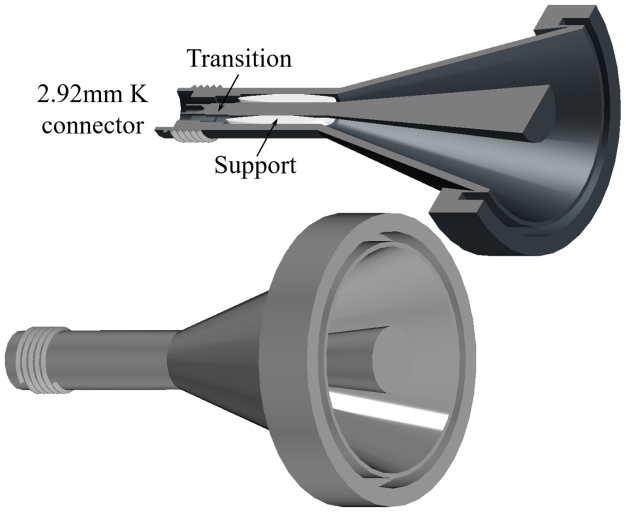


Fig. 1. Coaxial Horn's 3D model designed in *AutoCAD*

Elígia Simionato, UNESP, São João da Boa Vista - SP, e-mail: e.simionato@unesp.br; Rafael Abrantes Penchel, Seção Técnica de Apoio Acadêmico, UNESP, São João da Boa Vista - SP, e-mail: rafael.penchel@unesp.br; Sandro R. Zang, Department of Mechatronics and Telecommunication Engineering, UFSJ Campus Alto Paraopeba, Ouro Branco - MG, e-mail: sandrozang@gmail.com; Ivan Aldaya, Seção Técnica de Apoio Acadêmico, UNESP, São João da Boa Vista - SP, e-mail: ivan.aldaya@unesp.br.

## II. Coaxial Horn's Design

The complete model proposed for the coaxial horn (Fig. 2) features a Teflon structure to maintain the inner conductor's position in addition to the inner and outer conductors, deemed perfect electric conductors. This model can be divided into four regions of interest: a connector region that matches a female K connector's dimensions; a transition region to gradually modify the conductor's radii; a cylindrical region and a conic region that leads to the coaxial aperture. In addition, a corrugation is introduced at the aperture plane to minimize the interference in the antenna's radiation pattern [11]. Each of the described elements will be addressed in the following sections.

The horn's radiation pattern was explored seeking a stable radiation pattern throughout the whole $K_a$ frequency band, and ideally no nulls should occur before $\theta_F = 55°$, since that is the antenna's subreflector edge angle [14], [12], [13]. The reflection coefficient ($|S_{11}|$) was evaluated and used as the main benchmark for the horn's performance. All evaluations were conducted using ANSYS High Frequency Structure Simulator (HFSS), implementing the Finite Element Method (FEM) [16].

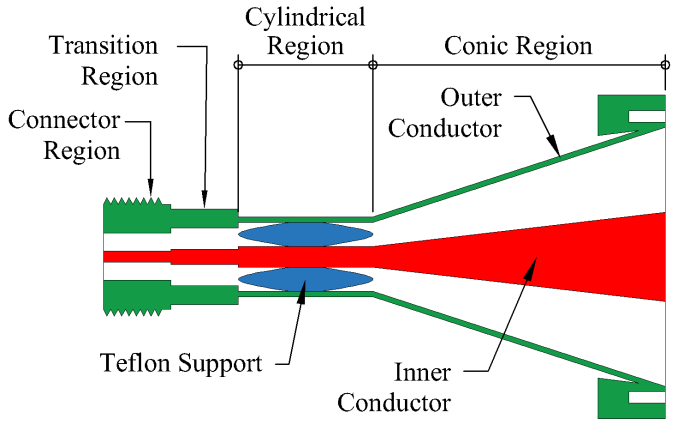


Fig. 2. Complete Model's Longitudinal Cut View

### A. Aperture Design

Fig. 3 illustrates a longitudinal cut in the coaxial horn's design (cylindrical and conical regions), with dimensions specified as a function of the wavelength ($\lambda_0$). The horn was designed for a frequency of $f = 28$GHz, therefore the wavelength value is $\lambda_0 = 10.714$mm.

The dimensions $r_a$, $r_b$ and $L$ are the ones in focus at this section. To analyze how they impact on the horn's performance and tailor these dimensions for an optimal outcome, parametric analysis was implemented as follows:

1. For $r_b = 0.80\lambda_0$, several values of $r_a$ between $0.25\lambda_0$ and $0.45\lambda_0$ were analyzed;
2. The same procedure was repeated for other values of $r_b$ within the range of $0.80\lambda_0$ to $0.96\lambda_0$ spaced by $0.04\lambda_0$;
3. The best result – the one that led to lower reflection coefficient and no nulls at $\theta < 55^o$ – among all the solutions (in steps 1. and 2.), was used to now analyze $L$ using variations within the range of $2.13\lambda_0$ to $2.21\lambda_0$ with a gap of $0.02\lambda_0$.

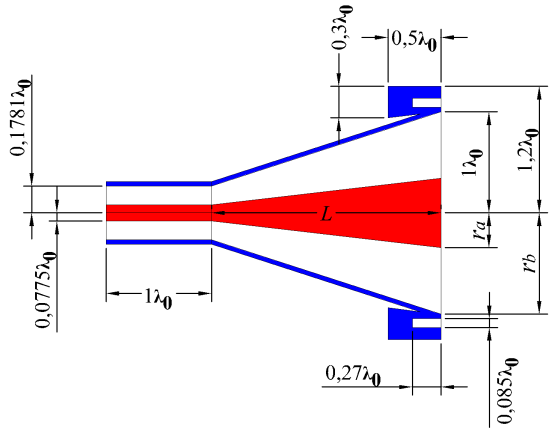


Fig. 3. Coaxial Horn's Dimensions as a function of $\lambda_0$

For the validation procedure, Fig. 4(a) presents the reflection coefficients for the reference horn (in red) [13], where $r_a = 0.35\lambda_0$, $r_b = 0.96\lambda_0$ and $L = 2.17\lambda_0$, and for the same horn (designed horn) simulated in Ansys Electronic Desktop (in blue), showing a good convergence of the results. Also in Fig. 4(b), the same convergence is observed for the radiation patterns, for 26, 28 and 40 GHz. For the parametric analysis, the best results for the modified horn were obtained when $r_a = 0.29\lambda_0$, $r_b = 0.96\lambda_0$ and $L = 2.15\lambda_0$. Figs. 4(a) and 4(d) illustrates these results for the reflection coefficients (in black) and radiation patterns, respectively.

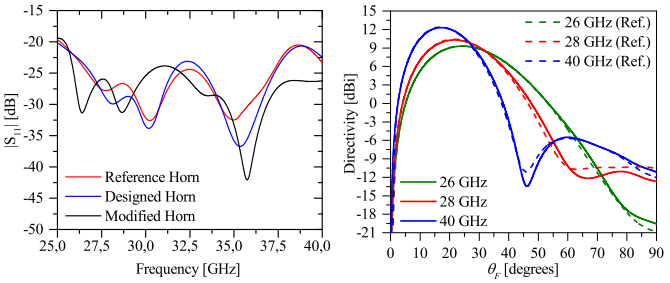


(a) Reflection Coefficient (b) Radiation Pattern

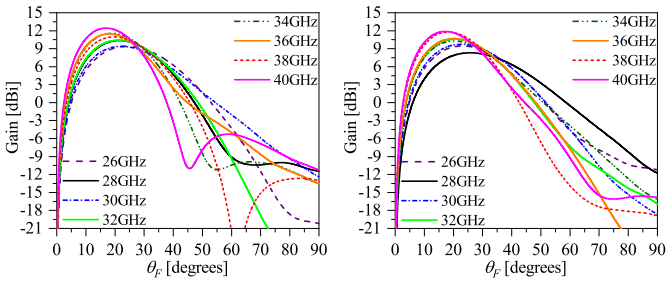


(c) Reference Horn Radiation Pattern (d) Modified Horn Radiation Pattern

Fig. 4. Outcome of the validation and aperture analysis process.

From reflection coefficients in Fig. 4(a) one notes that the parametric analysis led to a better performance compared with reference solution, especially for higher frequencies. Comparing the radiation pattern (Figs. 4(c) and 4(d)), one verifies that the outcome from parametric analysis positively influenced

this parameter, making the pattern more stable and avoiding nulls for $\theta_F < 55^o$ throughout the analyzed frequency band (25GHz – 40GHz). The values of the modified horn were the ones used for all further optimizations and analyses.

### B. Transition to a 2.92mm K Connector

To make the coaxial horn compatible with 2.92mm K connectors a transition region needs to be incorporated into the existing model. For this purpose we define a transition from the cylindrical region to a female 2.92mm K connector. To avoid reflection, it is desired that this transition occurs smoothly, and to accomplish that the feed end structure of the horn was divided into two – the connector region and the transition region – which can be seen in Fig. 5. In this way, the radii in the coaxial horn's cylindrical region's end can be gradually reduced to 2.92mm K connector dimensions.

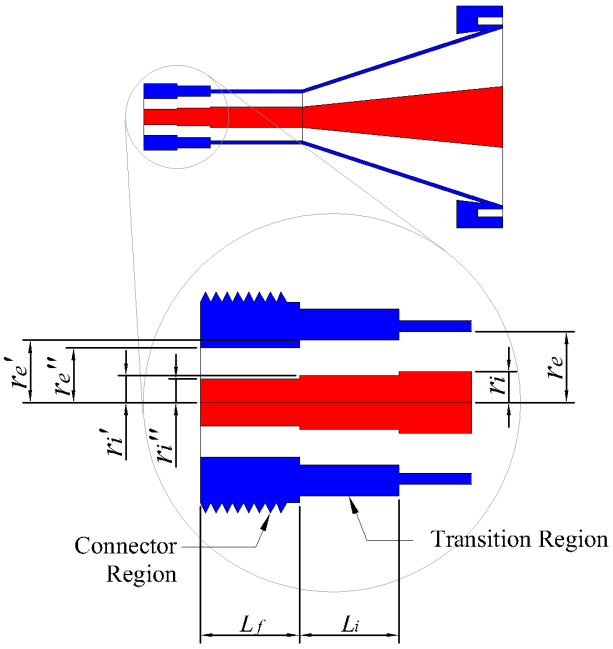


Fig. 5. Transition to 2.92mm K Connector

The radii that constitutes the connector region (outer $r_i''$ and inner $r_e''$ conductors, see Fig. 5) match the ones in a female K connector and, for the transition region, the inner conductor's radius ($r_i'$) as well as the dielectric's outer radius ($r_e'$) were calculated through the geometric mean between the connector region's radii and the ones at the horn's cylindrical region's feeding end ($r_i$ and $r_e$), as shown in Eq. (1). Additionally, the length of each of the transition regions ($L_f$ and $L_i$) is initially set to a fourth of the wavelength, with the total transition region's length being half the wavelength.

$$\begin{aligned} r_i' &= \sqrt{r_i \cdot r_i''} \\ r_e' &= \sqrt{r_e \cdot r_e''} \end{aligned} \tag{1}$$

To verify if a better performance was achievable, a parametric analysis was conducted considering the transition region's radii as well as the length of both transition and connector regions. For this analysis, a small range of values were tested, around $\pm 20\%$ of the original values. However, comparing the best results from this analysis with the initial outcome showed insignificant changes to the coaxial horn's performance, therefore the initial dimensions were maintained in upcoming analysis, where the dimensions in millimeters for $r_i$, $r_e$, $r_i'$, $r_e'$, $L_f$ and $L_i$ are described in Table I. Results of the transition region's analysis were compiled in Fig. 7.

### C. Dielectric Support for the Inner Conductor

Up until this point it was assumed that only air exists between the inner and outer conductor. However, a real implementation requires a structural support for the inner conductor that causes as little impact on the coaxial horn's performance as possible. To develop this support, several geometric shapes made of Teflon ($\epsilon_r = 2.1$) were tested positioned at the cylindrical region. As any modification to this region can cause little changes in the radiation pattern, only the $|S_{11}|$ parameter was matter of concern. Furthermore, the coaxial horn along with the mechanical support was analyzed, at first, without the transition region, as illustrated in Fig. 6(a).

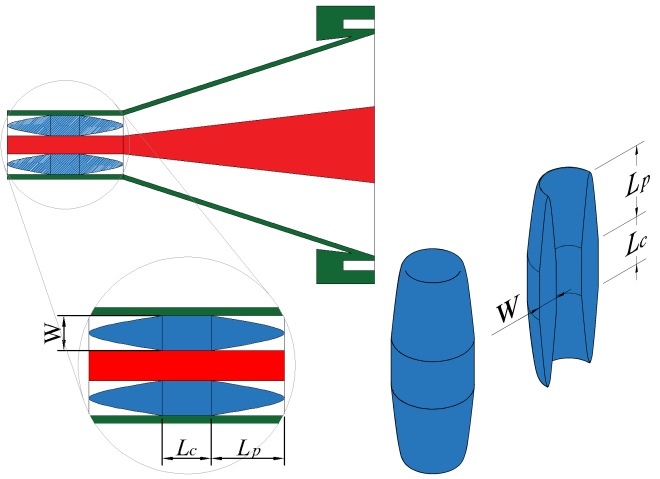


(a) Longitudinal Cut View (b) 3D View

Fig. 6. Teflon Geometry

The geometry illustrated in Fig. 6(b) was the one that achieved a reflection coefficient closest to the model without the Teflon support. This shape also represents fewer problems in manufacturing compared to the support presented in [11], as it can be easily placed between the two conductors.

To design the geometry on Fig. 6(b), two main shapes were used: a coaxial cylinder with its outer radius matching the dielectric radius and inner radius equal to the one on the inner conductor and a parabola-like shape created from Eq. (2).

$$\begin{cases} X(t) = t \\ Y(t) = 0 \\ Z(t) = L_p - \frac{L_p \cdot t^2}{W^2} \end{cases}, 0 \leq t \leq W \tag{2}$$

Where $L_p$ and $W$ are dimensions illustrated in Fig. 6 and X, Y and Z are directions in a 3D coordinate system.

When integrated in the simulation model the geometry's total length must not exceed the coaxial horn's cylindrical region's length (which measures $1\lambda_0$). Thereby, the parabola's equation was adjusted to depend only on the coaxial cylinder's length (Eq. (3)), not allowing overlapping objects that would lead to errors while running optimizations.

$$\begin{cases} X(t) = t \\ Y(t) = 0 \\ Z(t) = \frac{\lambda_0 - L_c}{2} - \frac{2\cdot(\lambda_0 - L_c)\cdot t^2}{W^2} \end{cases}, 0 \leq t \leq W \qquad (3)$$

Where $L_c$ is the dimension illustrated in Fig. 6.

Fig. 7 compiles results from the analysis described in Sections II-B and II-C.

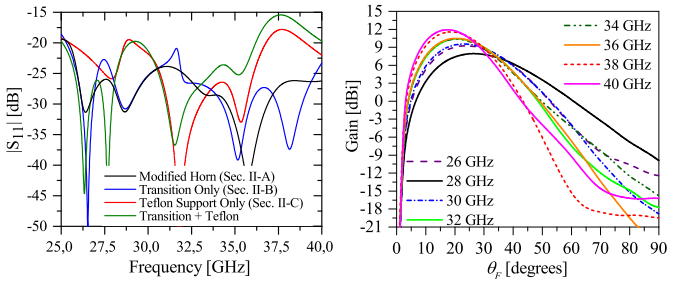


(a) Compared Reflection Coefficient (b) Complete Model's Radiation Pattern

Fig. 7. Results from analysis regarding transition region and Teflon support

Observing the reflection coefficients displayed in Fig. 7(a), one can notice that the transition and connector region did not significantly affect the horn's reflection coefficient. However, the Teflon support had a significant impact on the higher frequencies (36GHz – 40GHz) if compared with the modified horn's result (in black). The support geometry and its dimensions (see Table I) were chosen from a parametric analysis. The reflection coefficient (in red, see Fig. 7(a)) was considered, at this stage, sufficiently close to the desired goal ($|S_{11}| < -20$dB). Adding the transition and connector regions to the model with the Teflon support further degraded the reflection coefficient (in green), although it is still acceptable – for this initial solution –, the model would be optimized later on. In addition, as expected, the radiation pattern for the complete model (Fig. 7(b)) was not significantly affected by the modifications made in the cylindrical region and feeding end (see Fig. 4(d) for comparison).

TABLE I

PARAMETERS USED IN GA OPTIMIZATION

| Parameter | Initial Value | Optimized Value | Optimization Range | |
|---|---|---|---|---|
| | | | Min. Val. | Max. Val. |
| $L_i$ | 2.6785 | 1.448 | 1 | 4 |
| $L_f$ | 2.6785 | 2.808 | 1 | 4 |
| $r_i$ | 0.8304 | 0.6973 | 0.3 | 1.1 |
| $r_e$ | 1.9082 | 1.857 | 1.2 | 3 |
| $r'_i$ | 0.726 | 0.6038 | 0.3 | 0.8 |
| $r'_e$ | 1.678 | 1.466 | 0.8 | 2.5 |
| $L_c$ | 2.6785 | 2.18 | 1 | 4 |

Note: All values are in millimeters.

## III. NUMERICAL OPTIMIZATION

In the last step, we propose the coaxial horn's enhancement by Genetic Algorithm (GA) optimization. HFSS has an built-in GA optimizer which is an iterative random selection process that goes through a number of generations. Previously chosen coaxial horn's parameters, listed in Table I, will be referred to as variables and its values will be randomly selected within a determined range (see Table I) throughout the algorithm's execution. In this project the algorithm's default setup remained unchanged, which results in highly diverse individuals.

The GA process begins with a initial population of 30 individuals (possible solutions) and all of them are considered a potential parent.

The next step in the process is the Mating Pool where all of the potential parents go through a crossover and a mutation. The crossover type was set to Simulated Binary Crossover and all its default parameters were maintained, which will assure that all variables are mixed and two children cannot be exact clones of the parent that generated them. The mutation type was set to Polynomial Mutation with default parameters, which results in all children undergoing mutation.

After the Mating Pool, the process selects the 10 Pareto Front Survivors that are the very best individuals identified relative to the cost function, defined as $|S_{11}| \leq -20$. The algorithm then selects 30 individuals from the parents, the children and the Pareto front to comprise the next generation. At this stage, the selection of the best individuals is ten times more probable over the worst individual.

The described process will repeat until stopping criteria is met, in this case, it was a time limit of one week.

Seeking to reduce computational processing time, the parameters related to the conic/aperture region were not included in the optimization. Notwithstanding, those parameters were already adjusted through parametric analysis. Therefore, only parameters related to the cylindrical transition region, in addition to the connector region's length, were optimized using GA (see parameters in Table I), The initial dimensions for these structures are those resulting from the analysis previously made in Sections II-B and II-C. All relevant dimensions are described in Table I and illustrated in Fig. 5 and Fig. 6.

GA analysis' results revealed, among a total of 1328 iterations, nine iterations with cost zero. The best outcome of this process is compared with previously presented results and with the referenced results from [13] in Fig. 8. The optimized dimensions of the cylindrical transition and connector regions structures are described in Table I. The model used in simulations on HFSS along with the radiation pattern's 3D representation is illustrated in Fig. 9.

## IV. CONCLUSION

Operation of a TEM coaxial horn in mm-Waves was explored and optimized, primarily for the $K_a$ frequency range (26GHz – 40GHz). The study acquired better results, compared with referenced literature, in terms of reflection coefficient and a more stable radiation pattern throughout the entire frequency band. It also presented novel designs for a mechanical support to the inner conductor and for a

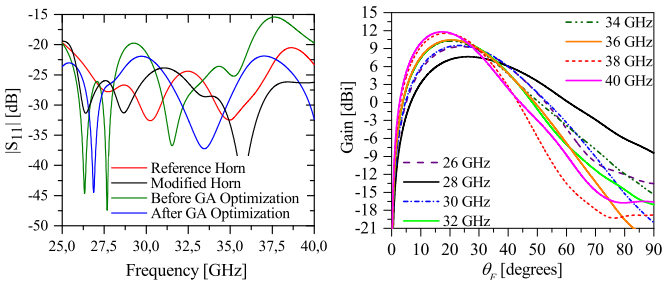


(a) Reflection Coefficient Comparison (b) Radiation Pattern

Fig. 8. Results for the final optimized model

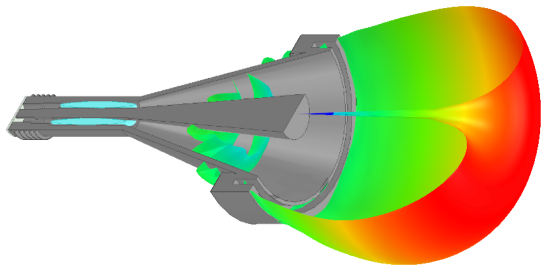

Fig. 9. Complete Model With 3D Radiation Pattern.

transition to a 2.92mm K connector which were successfully implemented in the optimized model, leading to a concept that offers little difficulties to the manufacturing process.

## ACKNOWLEDGMENT

This work was partially supported by the Brazilian agency FAPESP (Fundação de Amparo à Pesquisa do Estado de São Paulo), grant 2019/20209-8.

## REFERENCES

[1] NGMN Alliance, "5G White Paper", 2015. Accessed: Jan. 22, 2020. [Online]. Available: https://www.ngmn.org/wp-content/uploads/NGMN_5G_White_Paper_V1_0.pdf

[2] Z. Pi and F. Khan, "An introduction to millimeter-wave mobile broadband systems," in *IEEE Communications Magazine*, vol. 49, no. 6, pp. 101-107, June 2011. doi: 10.1109/MCOM.2011.5783993

[3] T. S. Rappaport et al., "Wireless Communications and Applications Above 100 GHz: Opportunities and Challenges for 6G and Beyond," in IEEE Access, vol. 7, pp. 78729-78757, 2019, doi: 10.1109/ACCESS.2019.2921522.

[4] Niu, Yong & Li, Yong & Jin, Depeng & Su, Li & Vasilakos, Athanasios. (2015). A Survey of Millimeter Wave (mm-Wave) Communications for 5G: Opportunities and Challenges. *Wireless Networks*. 21. 10.1007/s11276-015-0942-z.

[5] T. S. Rappaport et al., "Millimeter Wave Mobile Communications for 5G Cellular: It Will Work!," in *IEEE Access*, vol. 1, pp. 335-349, 2013. doi: 10.1109/ACCESS.2013.2260813

[6] M. Imbert, J. Romeu, M. Baquero-Escudero, M. Martinez-Ingles, J. Molina-Garcia-Pardo and L. Jofre, "Assessment of LTCC-Based Dielectric Flat Lens Antennas and Switched-Beam Arrays for Future 5G Millimeter-Wave Communication Systems," in IEEE Transactions on Antennas and Propagation, vol. 65, no. 12, pp. 6453-6473, Dec. 2017, doi: 10.1109/TAP.2017.2767821.

[7] Q. Jia, H. Xu, M. F. Xiong, B. Zhang and J. Duan, "Omnidirectional Solid Angle Beam-Switching Flexible Array Antenna in Millimeter Wave for 5G Micro Base Station Applications," in IEEE Access, vol. 7, pp. 157027-157036, 2019, doi: 10.1109/ACCESS.2019.2946372.

[8] A. I. Afifi, D. M. Elsheakh, A. B. Abdel-Rahman, A. Allam and S. M. Ahmed, "Dual Broadband Coplanar Waveguide-Fed Slot Antenna for 5G Applications," IEEE Transactions on Antennas and Propagation, vol. 65, no. 12, pp. 6904-6914, Dec. 2017, doi: 10.1109/TAP.2017.2759899.

[9] C. Mao, M. Khalily, P. Xiao, T. W. C. Brown and S. Gao, "Planar Sub-Millimeter-Wave Array Antenna With Enhanced Gain and Reduced Sidelobes for 5G Broadcast Applications," in IEEE Transactions on Antennas and Propagation, vol. 67, no. 1, pp. 160-168, Jan. 2019, doi: 10.1109/TAP.2018.2874796.

[10] R. A. Penchel, J. R. Bergmann and F. J. S. Moreira, "Main-Reflector Shaping of Omnidirectional Dual Reflectors Using Local Conic Sections," in IEEE Transactions on Antennas and Propagation, vol. 61, no. 8, pp. 4379-4383, Aug. 2013, doi: 10.1109/TAP.2013.2261571.

[11] S. Zang and J. Bergmann. Analysis of Omnidirectional Dual-Reflector Antenna and Feeding horn Using Method of Moments. *IEEE Transactions on Antennas and Propagation* , vol. 62, no. 3, pp. 1534-1538, Mar. 2014.

[12] Penchel, Rafael & Zang, Sandro & Bergmann, Jose & Moreira, Fernando. (2018). GO Shaping of Omnidirectional Dual-Reflector Antennas with Arbitrary Main-Beam Direction in Elevation Plane by Connecting Conic Sections. International Journal of Antennas and Propagation. 2018. 1-9. 10.1155/2018/1409716.

[13] R. Penchel, S. Zang, J. Bergmann and F. J. S. Moreira. Design of Wideband Omnidirectional Dual-Reflector Antennas in Millimeter Waves. *IEEE Antennas and Wireless Propagation Letters*, vol. 18, no. 5, pp. 906-910, May 2019, ISSN 1536-1225.

[14] F. J. da Silva Moreira and J. R. Bergmann, "Axis-Displaced Dual-Reflector Antennas for Omnidirectional Coverage With Arbitrary Main-Beam Direction in the Elevation Plane," in IEEE Transactions on Antennas and Propagation, vol. 54, no. 10, pp. 2854-2861, Oct. 2006, doi: 10.1109/TAP.2006.882181.

[15] International Telecommunication Union - Radio-communication sector, "Minimum requirements related to technical performance for IMT-2020 radio interface(s)", ITU, Geneva, Rep. ITU-R M.2410-0, 2017.

[16] M. N. O. Sadiku. Numerical Techniques in Electromagnetics. 2nd ed. CRC Press. 2001.